In vivo diffusion-weighted MRS using semi-LASER in the human brain at 3 T: methodological aspects and clinical feasibility

Genovese, G.; Marjanska, M.; Auerbach, E.J.; Cherif, L.Y.; Ronen, I.; Lehericy, S.; Branzoli, F.

Received: 26 April 2019 | Revised: 18 September 2019 | Accepted: 7 October 2019

DOI: 10.1002/nbm.4206

SPECIAL ISSUE RESEARCH ARTICLE

WILEY NMR IN BIOMEDICINE

In vivo diffusion-weighted MRS using semi-LASER in the human brain at 3 T: Methodological aspects and clinical feasibility

Guglielmo Genovese[1,2] | Małgorzata Marjańska[3] | Edward J. Auerbach[3] | Lydia Yahia Cherif[1,2] | Itamar Ronen[4] | Stéphane Lehéricy[1,2] | Francesca Branzoli[1,2]

[1] Centre de NeuroImagerie de Recherche (CENIR), Institut du Cerveau et de la Moelle épinière (ICM), Paris, France

[2] UPMC Université Paris 06 UMR S 1127, Sorbonne Universités, Inserm U 1127, CNRS UMR 7225, Paris, France

[3] Center for Magnetic Resonance Research and Department of Radiology, University of Minnesota, Minneapolis, MN, USA

[4] C. J. Gorter Center for High Field MRI, Department of Radiology, Leiden University Medical Center, Leiden, The Netherlands

Correspondence
Francesca Branzoli, PhD, Institut du Cerveau et de la Moelle épinière (ICM), Hôpital Pitié-Salpetrière, 47 boulevard de l'Hôpital, CS 21414, 75646. Paris Cedex 13, France.
Email: francesca.branzoli@icm-institute.org

Funding information
Infrastructure d'avenir en Biologie Santé, Grant/Award Number: ANR-11-INBS-0006; Institut des neurosciences translationnelle, Grant/Award Number: ANR-10-IAIHU-06; NIH, Grant/Award Numbers: BTRC P41 EB015894, P30 NS076408, BTRC P41 EB015894

Diffusion-weighted (DW-) MRS investigates non-invasively microstructural properties of tissue by probing metabolite diffusion in vivo. Despite the growing interest in DW-MRS for clinical applications, little has been published on the reproducibility of this technique. In this study, we explored the optimization of a single-voxel DW-semi-LASER sequence for clinical applications at 3 T, and evaluated the reproducibility of the method under different experimental conditions. DW-MRS measurements were carried out in 10 healthy participants and repeated across three sessions. Metabolite apparent diffusion coefficients (ADCs) were calculated from mono-exponential fits (ADC_{exp}) up to b = 3300 s/mm^2, and from the diffusional kurtosis approach (ADC_K) up to b = 7300 s/mm^2. The inter-subject variabilities of ADCs of *N*-acetylaspartate + *N*-acetylaspartylglutamate (tNAA), creatine + phosphocreatine, choline containing compounds, and *myo*-inositol were calculated in the posterior cingulate cortex (PCC) and in the corona radiata (CR). We explored the effect of physiological motion on the DW-MRS signal and the importance of cardiac gating and peak thresholding to account for signal amplitude fluctuations. Additionally, we investigated the dependence of the intra-subject variability on the acquisition scheme using a bootstrapping resampling method. Coefficients of variation were lower in PCC than CR, likely due to the different sensitivities to motion artifacts of the two regions. Finally, we computed coefficients of repeatability for ADC_{exp} and performed power calculations needed for designing clinical studies. The power calculation for ADC_{exp} of tNAA showed that in the PCC seven subjects per group are sufficient to detect a difference of 5% between two groups with an acquisition time of 4 min, suggesting that ADC_{exp} of tNAA is a suitable marker for disease-related intracellular alteration even in small case–control studies. In the CR, further work is needed to evaluate the voxel size and location that minimize the motion artifacts and variability of the ADC measurements.

Abbreviations: ADC, apparent diffusion coefficient; C_R, coefficient of repeatability; Cr, creatine; CR, corona radiata; CRLB, Cramér-Rao lower bound; C_V, coefficient of variation; δ, diffusion gradient duration; DW, diffusion weighted; GM, gray matter; mIns, *myo*-inositol; PCC, posterior cingulate cortex; PCr, phosphocreatine; rANOVA, repeated analysis of variance; SD, standard deviation; SNR, signal-to-noise ratio; tCho, choline containing compounds; tCr, creatine + phosphocreatine; t_d, diffusion time; tNAA, *N*-acetylaspartate + *N*-acetylaspartylglutamate; VAPOR, variable power with optimized relaxation delays; VOI, volume of interest; WM, white matter

KEYWORDS

diffusion, metabolites, optimization, power calculation, repeatability, reproducibility

1 | INTRODUCTION

Diffusion-weighted (DW-) MRS explores metabolic and microstructural properties of healthy and diseased brains by probing the diffusion of several metabolites in vivo.[1-4] Similarly to conventional MRS, DW-MRS exploits the specific compartmentalization of metabolites in different cell types, thus enabling differentiation between physiological or pathological mechanisms affecting brain tissue. The addition of magnetic field gradient pulses to MRS sequences allows sensitization of the NMR signal to diffusion, and quantification of metabolite displacement in tissue at a given time-scale. From metabolite diffusion measures, it is possible to derive information on cell size and morphology,[5-8] as well as on the properties of the intracellular environment, such as viscosity and molecular crowding.[9] When combined with DW imaging techniques, DW-MRS provides a unique way to differentiate between axonal degeneration, glial activation, and demyelination.[10-13] Although very promising, the application of DW-MRS techniques in clinical studies is challenging due to the intrinsic low signal-to-noise ratio (SNR) of metabolites, especially when the spectra are acquired at high diffusion-weightings. To overcome the issue of low SNR at high *b*-values, DW-MRS often requires long acquisition times, which are not always feasible in a clinical setting. In addition, obtaining robust and reproducible DW-MRS data is hampered by the high sensitivity of this technique to bulk and physiological motion, affecting both the phase and the amplitude of individual DW-MRS acquisitions. These deleterious effects increase dramatically the variance in DW-MRS calculated measures, resulting in low reproducibility and in significantly overestimated diffusion coefficients.[4,14] All these factors point towards the need for accurate post-processing procedures, in addition to effective acquisition strategies.

Currently, the most commonly used techniques for DW-MRS are based on stimulated echo acquisition mode (STEAM),[15] point-resolved spectroscopy (PRESS),[16] and localization by adiabatic selective refocusing (LASER),[17] with magnetic field gradient pulses added in variable configurations for diffusion sensitization.[4] DW-STEAM allows for long diffusion times keeping a short echo time (T_E), and is thus ideal for exploration of the time dependence of metabolite diffusion.[5,9,18,19] DW-STEAM has also been shown to better quantify diffusion of *J*-coupled metabolites compared with DW-PRESS.[20] Spin-echo sequences provide higher SNR for a given T_E, and, when equipped with a full bipolar diffusion gradient scheme, they allow maximization of the achievable *b*-value. These characteristics are highly beneficial, especially for applications on clinical scanners, where the maximum available gradient strength is limited by hardware constraints. Fully adiabatic LASER[17] or partially adiabatic semi-LASER[21] coupled with diffusion gradients (DW-semi-LASER) have the additional advantages of reducing signal losses related to B_1 field inhomogeneities and lower chemical shift displacement error compared with STEAM and PRESS sequences with standard RF pulses.[22] Despite the increasing number of studies reporting different applications of DW-MRS to investigate brain tissue, and the importance of the evaluation of the reliability of the method for a study design, to our knowledge only two reports so far have tested the reproducibility of DW-MRS methods. In contrast to our study, one of these reports focused on a specific model of metabolite diffusion in the human corpus callosum employing a DW-PRESS sequence at both 3 T and 7 T.[23] In the second report, a DW-STEAM sequence was employed to measure metabolite apparent diffusion coefficients (ADCs) at 3 T, and the reproducibility of the method was tested in the subcortical white matter (WM) in a small group of three subjects.[24] Yet, the long acquisition time employed in this study is not suitable for clinical applications.

The goal of the present study was to optimize the acquisition and post-processing procedures for single-voxel DW-MRS experiments, and to evaluate the feasibility of clinical studies using a DW-semi-LASER sequence at 3 T. To this aim, we report the variability of ADCs of *N*-acetylaspartate + *N*-acetylaspartylglutamate (tNAA), creatine + phosphocreatine (tCr), choline containing compounds (tCho), and *myo*-inositol (mIns), measured using DW-semi-LASER in two brain regions containing mostly gray matter (GM) or WM. In order to explore the impact of a series of methodological issues on the variability of metabolite ADCs, the reproducibility of the diffusion measures was evaluated for different experimental conditions across repeated measurements of the same subject, and across subjects. In particular, the effect of physiological motion on the DW-MRS signal and the importance of cardiac gating and peak thresholding to account for signal amplitude fluctuations were investigated. The ADCs were calculated using mono-exponential functions up to moderately high *b*-values (b = 3300 s/mm^2), as well as using a kurtosis model for measurements up to high *b*-values (b = 7300 s/mm^2). Finally, based on the variance of the metabolite ADCs, we provide power calculations that can be used for planning clinical studies, and discuss the suitability of DW-MRS for case–control studies in disease populations.

2 | MATERIAL AND METHODS

2.1 | Human subjects

Ten healthy volunteers (seven males, three females; mean age ± standard deviation (SD) 25 ± 3 years, range 20–29 years) participated in this study. Each subject underwent the same MRI/MRS examination during three different sessions (S1, S2, and S3), each on a different day, with a

maximum delay between sessions of three weeks. All subjects provided informed consent according to local procedures prior to the study. The study was approved by the local ethics committee.

2.2 | MRI hardware

All subjects were scanned on a 3 T whole-body Siemens MAGNETOM Prisma Fit MRI scanner (Siemens Medical Solutions, Erlangen, Germany). The scanner was equipped with gradient coils capable of reaching 80 mT/m on each of the three orthogonal axes. The standard RF body-coil was used for excitation and a 64-channel receive-only head coil for reception.

2.3 | MRI/DW-MRS protocol

At the beginning of each scan, three-dimensional T_1-weighted magnetization-prepared rapid gradient echo images (field of view, 256 (anterior–posterior) × 256 (foot-head) × 231 (right–left) mm^3; isotropic resolution, 0.9 mm; T_R/T_E, 2300/2.08 ms; total acquisition time, 5 min 17 s) were acquired to position the spectroscopic volumes of interest (VOIs) and to perform tissue segmentation.

The DW-MRS acquisitions were performed using a single-voxel semi-LASER sequence with diffusion gradients added in a bipolar configuration, as shown in Figure 1. Using the bipolar configuration of the diffusion gradients minimizes eddy currents as well as cross terms between the diffusion gradients and gradients rising from inhomogeneities of the B_0 field.[25] DW-MRS data were acquired in two VOIs of 20 × 20 × 20 mm^3 located in the posterior cingulate cortex (PCC), from here on referred to as VOI_{PCC} (Figure 2A), and in the corona radiata (CR), from here on referred to as VOI_{CR} (Figure 2C). In the CR, data were acquired in eight subjects also in a smaller VOI (VOI'_{CR}) of 15 (foot-head) × 20 (anterior–posterior) × 15 (right–left) mm^3, with the same center as VOI_{CR} (in two subjects it was not possible to perform the measurement in VOI'_{CR} for technical reasons). For all VOIs, sequence parameters were T_E = 120 ms, spectral width = 3 kHz and number of complex points = 2048. All resonances were excited using a slice-selective 90° pulse (pulse length of 2.52 ms) followed by two pairs of slice-selective adiabatic refocusing pulses in the other two dimensions (HS1, R = 24, pulse length 7 ms). The 64-channel signals were combined on-line using a reference water scan, after appropriate phase adjustment and amplitude weighting of each channel for optimal SNR combination. All acquisitions were synchronized with cardiac cycle using a pulse-oximeter device, in order to start each acquisition every three heart beats, while maintaining a minimum T_R of 2.5 s. To verify the effect of cardiac gating on signal fluctuations, an additional acquisition was performed in one subject without a pulse-oximeter device at T_R = 2.5 s. Diffusion-weighting was applied in three orthogonal directions (dir_1 = [1, 1, −0.5], dir_2 = [1, −0.5, 1], dir_3 = [−0.5, 1, 1] in the VOI coordinate system) with diffusion gradient duration (δ) = 18 ms, diffusion time (t_d) = 60 ms and three increasing gradient strengths resulting in the b-values b_1 = 850, b_2 = 3300 and b_3 = 7300 s/mm^2. The b-values were calculated using the chronograms of the pulse sequence, and therefore accounted for all gradients present in the sequence, including slice-selective and crusher gradients. A non-DW condition with diffusion gradient amplitude set to zero was also acquired: b_0 = 11 s/mm^2, where the small b-value originates from the slice-selective and crusher gradients. Forty averages were collected for each diffusion-weighting condition and saved as individual free induction decays for further post-processing. Water suppression was performed using variable power with optimized relaxation delays (VAPOR) and outer volume suppression.[26] The delays used for VAPOR were 150, 100, 146, 105, 106, 68, 80, and 22 ms.[27] Unsuppressed water reference scans were acquired from the same VOIs using the same parameters as water suppressed spectra for eddy current corrections. B_0 shimming was performed using a fast automatic shimming technique with echo-planar signal trains utilizing mapping along projections, FAST (EST) MAP.[28]

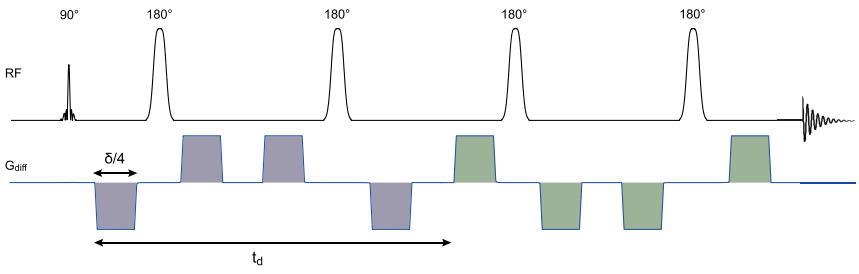

FIGURE 1 Schematic diagram of the DW-semi-LASER sequence. The RF pulses are shown together with the DW gradients, but without slice-selective or crusher gradients. t_d is the time between the first lobe of the dephasing diffusion gradient group (in gray) and the first lobe of the re-phasing diffusion gradient group (in green). The total gradient duration δ corresponds to the sum of the durations of four lobes, and is identical for dephasing and re-phasing groups

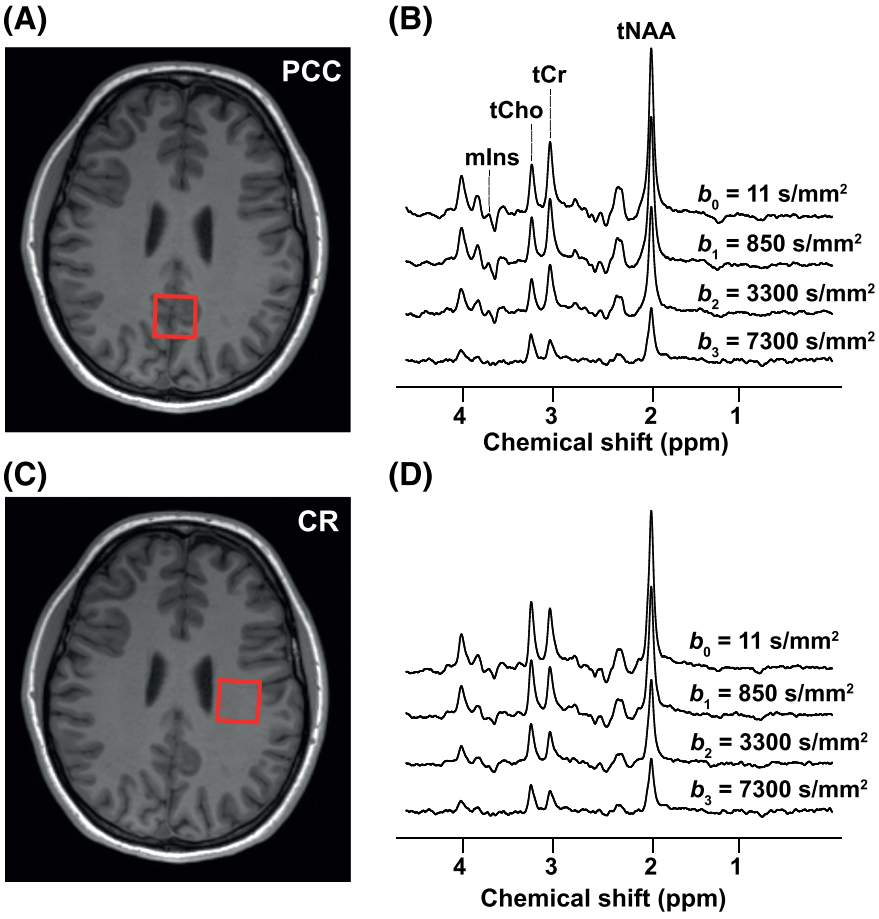

FIGURE 2 DW spectra and VOIs. The locations of the VOIs in the PCC (a) and the CR (C) are shown on T_1-weighted images together with examples of DW spectra acquired at different *b*-values in VOI_{PCC} (B) and VOI_{CR} (D)

The total DW-MRS scan time for VOI_{PCC} and VOI_{CR} was about 17 min for each VOI. In VOI'_{CR}, an additional shorter acquisition was performed using only b_0 and b_2 (the latest applied in the three orthogonal directions) and 24 averages per diffusion condition (about 4 min), to evaluate, under these experimental conditions, the effect of voxel size on data variability.

2.4 | Spectral processing

All spectra were processed with an in-house written routine in MATLAB release R2016b (MathWorks, Natick, MA, USA). DW-MRS data were first corrected for eddy currents using water reference scans. Zero-order phase fluctuations and frequency drifts were corrected on single averages before summation using an area minimization and penalty algorithm and a cross-correlation algorithm, respectively.[29] A peak-thresholding procedure was applied, for each diffusion condition, to discard the single averages with artifactual low SNR caused by non-translational tissue motion, which is not justified by gaussian noise alone (see Supplementary Material S1). The remaining spectra, for each condition, were averaged. Finally, the averaged spectra were analyzed with LCModel[30] for metabolite quantification. The basis set was simulated with an in-house written routine in MATLAB based on the density matrix formalism[31] and using previously reported chemical shifts and *J*-couplings.[32,33] The basis set included alanine, ascorbate, aspartate, creatine (Cr), γ-aminobutyric acid, glucose, glutamate, glutamine, glutathione, glycerophosphorylcholine, mIns, lactate, *N*-acetylaspartate (NAA), *N*-acetylaspartylglutamate, phosphocreatine (PCr), phosphorylcholine, phosphorylethanolamine, *scyllo*-inositol, and taurine. Independent spectra for the CH_3 and CH_2 groups of NAA, Cr, and PCr were simulated and included in the basis set.

2.5 | Metabolite diffusion measures

Based on the LCModel data, metabolite diffusivity properties for tNAA, tCr, tCho, and mIns were calculated in each VOI. ADCs were computed assuming a mono-exponential decay of the signal up to b_2 (Figure 3) in each diffusion direction:

$$\ln\left[\frac{S^i(b)}{S_0}\right] = -b \cdot ADC^i_{exp} \quad (1)$$

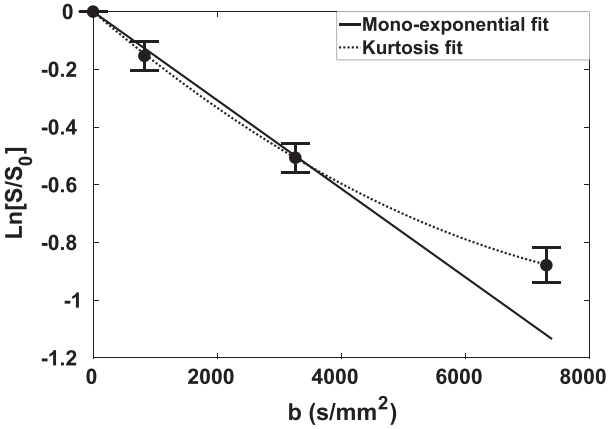

FIGURE 3 tNAA attenuation curves. Natural logarithm of tNAA normalized signal decay plotted as a function of *b*-value. The attenuation curve was fitted to a mono-exponential function (solid line) up to b_2 = 3300 s/mm^2 and to a kurtosis model (dashed line) up to b_3 = 7300 s/mm^2

where $S^i(b)$ is the signal measured at a given *b*-value in direction *i*, S_0 is the signal measured at b_0, and ADC^i_{exp} is the corresponding apparent diffusion coefficient estimated in direction *i*. Since the signal decay obtained up to b_3 was not mono-exponential, the signal decay up to this *b*-value was evaluated using the kurtosis approach[34,35] (Figure 3):

$$\ln\left[\frac{S^i(b)}{S_0}\right] = -b\cdot ADC^i_K + \frac{K^i}{6}\left(b\cdot ADC^i_K\right)^2 \quad (2)$$

where ADC^i_K is the apparent diffusion coefficient for direction *i* and K^i is the kurtosis parameter in the same direction. The quality of both mono-exponential and kurtosis fits up to b_3 was assessed using a chi-square (χ^2) goodness-of-fit test for the residuals, using the Cramér-Rao lower bounds (CRLBs) provided by LCModel as SDs for the metabolite signal amplitudes.

2.6 | Inter-subject variability

The inter-subject variability of the diffusion measures was evaluated for all four metabolites and all VOIs. Coefficients of variation (C_V) were calculated as ratios between SDs and mean values of the diffusion parameters. SDs and mean values were estimated across subjects for each session separately, as well as across subjects and sessions, and were consequently used for the C_V evaluations.

First the effects of peak thresholding, diffusion-weighting direction, and VOI size on the mean values and variability of tNAA diffusion measures were evaluated. Subsequently the C_V values were calculated for metabolite ADC_{exp}, ADC_K, and *K* estimated using peak thresholding and averaged over three diffusion directions.

2.7 | Intra-subject variability

The intra-subject variability analysis was carried out on ADC_{exp}, ADC_K, and *K* of tNAA and tCho derived from VOI_{PCC} and VOI_{CR}. The dependence of the intra-subject variability of the diffusion measures on the acquisition time was evaluated by computing the diffusivity parameters for each subject, considering different diffusion-weighting schemes and different numbers of spectral averages per diffusion condition. For this purpose, a bootstrapping subsampling procedure was used: the datasets from each session were randomly resampled with replacement prior to averaging. Each subset consisted respectively of 10, 15, 20, 25, 30, 35, and 40 averages per diffusion condition (e.g. per *b*-value and diffusion direction). In addition, the ADC_{exp} and their variabilities were estimated from different diffusion-weighting schemes: scheme $b_{[0,1,2]}$ employs b_0, b_1, and b_2; scheme $b_{[0,2]}$ employs b_0 and b_2; scheme $b_{[0,1]}$ employs b_0 and b_1. The *K* were estimated using all *b*-values, b_0, b_1, b_2, and b_3 (scheme $b_{[0-3]}$).

For each resampled subset, the averaged spectra needed for calculation of the diffusion metrics were obtained. The bootstrapping procedure was repeated 200 times for each subset size to obtain a bootstrap population. From the bootstrap populations, mean values and SDs of the diffusivity parameters were obtained and utilized for intra-subject C_V calculations.

2.8 | Reproducibility and sample size analysis

A one-way repeated analysis of variance (rANOVA) model (MATLAB release R2016b) was performed to evaluate the within-subject variability (σ) of metabolite ADC_{exp} averaged over the diffusion directions. σ was used for repeatability coefficient (C_R) and power/sample size calculations. C_R within the 95% confidence interval was defined as $C_R = 1.96\sqrt{2}\sigma$.[36]

Power calculations were performed to estimate the necessary sample size to detect a difference (Δ) in tNAA ADC_{exp}, and K between two groups. These were based on a two-sided test with significance level $\alpha = 0.05$ ($z_{1-\alpha/2} = 1.96$), and a power of 80% ($1-\beta = 0.80$, $z_{1-\beta} = 0.84$):

$$n = \frac{\sigma^2 \left(z_{1-\alpha/2} + z_{1-\beta}\right)^2}{\Delta^2} \tag{4}$$

It was assumed that the means were normally distributed and the variances of the two groups were the same ($\sigma_1 = \sigma_2 = \sigma$).

3 | RESULTS

3.1 | DW spectra quality

Representative DW spectra acquired in VOI_{PCC} and VOI_{CR} of one subject at all b-values applied in one diffusion gradient direction (dir_1) are shown in Figure 2B and 2D, respectively. The CRLBs of tNAA calculated from all subjects, all b-values, all directions, and all VOIs ranged from 2 to 7%, while the CRLBs of tCr and of tCho ranged from 3 to 12%. The CRLBs of mIns were lower than 20% for all b-values in VOI_{PCC} and lower than 35% for all b-values up to b_2 in VOI_{CR}, whereas for b_3 in VOI_{CR} they were higher than 50% for 5 out of 30 datasets and were therefore excluded from the kurtosis analysis. In VOI'_{CR}, the CRLBs of mIns at b_2 were greater than 35% for more than half of the datasets; therefore, these signals were not considered for further analysis. The mean SNR, based on the tNAA peak (averaged over all sessions and DW directions), was 24 for b_0 and 14 for b_3 in VOI_{PCC}. In VOI_{CR}, the mean SNR was 23 for b_0 and 9 for b_3. Both in VOI_{PCC} and in VOI_{CR}, no differences in SNR were observed between different DW directions. The SNRs were considerably lower in VOI'_{CR} than in VOI_{CR} for each direction and both b-values: SNR = 14 for b_0 and SNR = 8 for b_2.

The linearity of the signal logarithm attenuation for the acquisition scheme $b_{[0-2]}$ was very good for all metabolites in both GM and WM ($R^2 > 0.9$ for all fits). In contrast, for the acquisition scheme $b_{[0-3]}$ a significant deviation from linearity was observed in about 30% of the fits ($p < 0.05$ for the χ^2 goodness-of-fit test for the residuals), and the signal decay was better fitted by the kurtosis model: for all fits, the null hypothesis of the χ^2 goodness-of-fit test was accepted with $p > 0.9$.

Tissue segmentation results showed that the average WM fraction was 88 ± 4% in VOI_{CR} and 94 ± 4% in VOI'_{CR}, while the average GM fraction in VOI_{PCC} was 72 ± 5%.

3.2 | Effect of acquisition strategy and post-processing on the variability of the diffusion measures

3.2.1 | Cardiac gating

Figure 4A and 4B shows the SNR of tNAA for single averages (40 averages for each diffusion condition) with and without cardiac gating, respectively. Mean SNRs derived with and without cardiac gating at b_1, b_2, and b_3 were plotted for each diffusion direction (Figure 4C). The SNRs were normalized to the SNR calculated at $b_0 = 11$ s/mm^2 (SNR_0), in order to remove effects due to fluctuations in T_R in the acquisitions with cardiac gating. The mean SNRs of the spectra acquired with cardiac gating were higher for each b-value and diffusion condition. The associated SDs were slightly lower with heartbeat trigger, except for b_1 in dir_2.

3.2.2 | Peak thresholding

The average numbers of spectra rejected after peak thresholding were 3 for b_0 and b_1, 4 for b_2, and 5 for b_3 in VOI_{PCC}, and 2, 6, 10, and 12, respectively, in VOI_{CR}. In VOI'_{CR}, 1 and 2 spectra on average were rejected for b_0 and b_2, respectively.

Figure 5 shows an example of 40 averages acquired at b_3 in VOI_{CR}, plotted without post-processing (A), after eddy current, phase, and frequency corrections (B), and after peak thresholding (C).

Figure 6 shows ADC_{exp} (A, B), ADC_K (C, D), and K (E, F) of tNAA measured in VOI_{PCC} and VOI_{CR} for each diffusion direction, from all subjects and all sessions, with and without peak thresholding. In VOI_{PCC}, decreases in both the mean values and the variability of ADC_{exp} were observed when peak thresholding was applied (Figure 6A). The C_V of ADC_{exp} decreased after peak thresholding by 26% in dir_1, 14% in dir_2, and 35% in dir_3. In contrast, no differences in the C_V of ADC_K were observed in any of the three directions when peak thresholding was applied. In VOI_{CR} the mean values and the C_V of ADC_{exp} decreased strongly in each direction when peak thresholding was applied: 33% in dir_1, 41% in dir_2, and 39% in dir_3 (Figure 6B). Similarly, in this region the C_V of ADC_K decreased by 25%, 36%, and 21% in dir_1, dir_2, and dir_3, respectively (Figure 6D). In both VOIs, no differences in the variability of K were observed when peak thresholding was applied (Figure 6E and 6F). The diffusion metrics and their C_V reported from here on were calculated with peak thresholding.

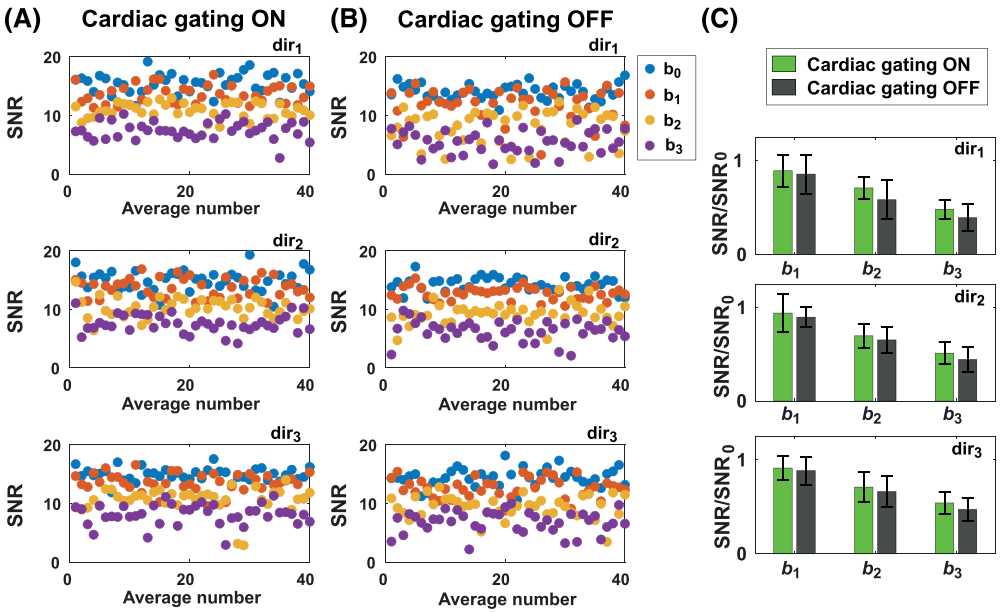

FIGURE 4 Effect of cardiac gating on tNAA SNR. A, B, tNAA SNR calculated for single averages in one subject at all *b*-values and DW directions with (A) and without (B) cardiac gating. C, comparison of average SNR at different *b*-values (b_1, b_2, and b_3) and directions (dir_1, dir_2, dir_3) obtained with and without cardiac gating. The reported SNRS were normalized to the SNR calculated at b_0 (SNR_0), in order to remove effects due to fluctuations in T_R in the acquisitions with cardiac gating. Error bars represent standard deviations

3.2.3 | DW direction

In VOI_{PCC}, the variability of ADC_{exp} and ADC_K of tNAA was very similar for the three directions: mean C_V = 9% and 12% for the two metrics, respectively (Figure 6A and 6C). In contrast, in VOI_{CR}, the variabilities of ADC_{exp}, ADC_K, and *K* of tNAA (C_V = 10%, 14%, and 27%, respectively) were lower in dir_3 with respect to the other two directions (C_V = 18%, 22%, and 38% for both dir_1 and dir_2) (Figures 6B, 6D and 6F).

3.2.4 | Voxel size

Figure 7 shows the ADC_{exp} of tNAA derived in VOI_{CR} and VOI'_{CR}, plotted for all subjects and all sessions, and for each DW direction. In both voxels, ADC_{exp} values were estimated using scheme $b_{[0,2]}$ and 24 averages per diffusion condition. In contrast to VOI_{CR}, the variability estimated from VOI'_{CR} did not present any significant dependence on the diffusion-weighting direction (averaged C_V = 16%). The C_V values calculated in VOI'_{CR} in dir_1 and dir_2 dropped by 19% with respect to those derived from VOI_{CR} in the same directions, while they were comparable in dir_3. Similar behavior with respect to peak thresholding, DW direction, and VOI size was observed for the variability of tCr, tCho, and mIns diffusion measures (data not shown).

3.3 | Inter-subject variability

tNAA, tCr, tCho, and mIns diffusivity measures averaged across diffusion directions and subjects are reported for each session, with the associated SD and C_V values, in Tables 1 and 2, for VOI_{PCC} and for VOI_{CR} and VOI'_{CR}, respectively. No significant differences in diffusivity measures of the metabolites across the sessions were observed (rANOVA).

In VOI_{PCC}, the C_V values estimated for ADC_{exp} and ADC_K of all metabolites ranged from 6% to 14% and from 8% to 18%, respectively, while the C_V of *K* ranged from 11% to 34% (Table 1). In VOI_{CR}, the C_V of ADC_{exp} and ADC_K were higher than those calculated in VOI_{PCC}, ranging from 7% to 32%, while the C_V of *K* ranged from 15% to 38% (Table 2). Finally, in the VOI'_{CR} the C_V of tNAA, tCr, and tCho ADC_{exp} ranged from 8% to 19% (Table 2). In Figure 8, all diffusivity measures computed for all metabolites from all subjects and all sessions for the two VOIs are shown.

3.4 | Effect of acquisition time on intra-subject variability

Figure 9 shows the C_V of ADC_{exp} and *K* of tNAA calculated as a function of the number of averages acquired in VOI_{PCC} (Figure 9A and 9C) and in VOI_{CR} (Figure 9B and 9D), based on data resampling from all subjects and sessions. The C_V of ADC_{exp} of tNAA was evaluated for different

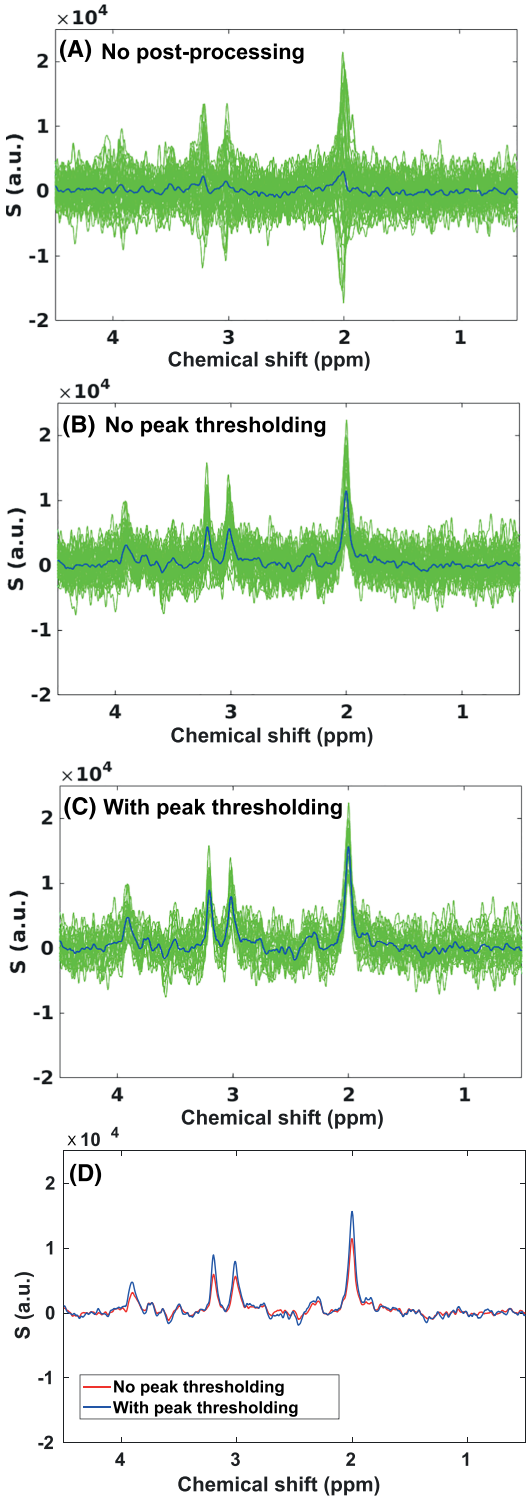

FIGURE 5 Post-processing. A-C, example of 40 averages acquired with cardiac gating at b_3 from VOI_{CR}, plotted without post-processing (A), after post-processing without peak thresholding (eddy current, phase, and frequency corrections) (B), and after post-processing with peak thresholding (C). Blue lines correspond to the average spectra. In this example, fourteen spectra had artifactual low SNR and were discarded. D, comparison of the average spectra obtained with and without peak thresholding

acquisition schemes: $b_{[0,1,2]}$, $b_{[0,2]}$, and $b_{[0,1]}$. In both VOIs, C_V < 10% for ADC_{exp} of tNAA was observed with more than 60 and 90 averages acquired with schemes $b_{[0,2]}$ and $b_{[0,1,2]}$, respectively, corresponding to scanning times of 3 and 4 min. Notably, the C_V achieved for $b_{[0,2]}$ with 160 averages (scanning time of 7 min) and for $b_{[0,1,2]}$ with a total of 280 spectra (scanning time of 12 min) were comparable (~5% in VOI_{PCC} and ~7% in VOI_{CR}). Much higher values of C_V (>15%) were observed for $b_{[0,1]}$ in both VOIs, as expected given the low b-value utilized for this

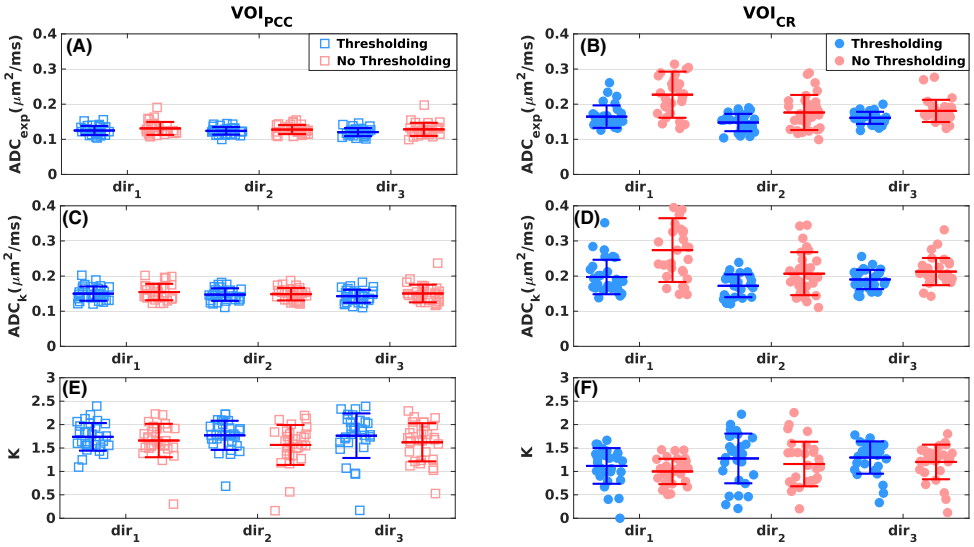

FIGURE 6 Effect of peak thresholding on the variability of tNAA diffusion measures. Diffusivity measures of tNAA derived in VOI_{PCC} (A, C, E) and VOI_{CR} (B, D, F) from all subjects and sessions, displayed separately for each diffusion direction. Mean values (central bars) and SDs (outer bars) are plotted for each parameter and direction

scheme. The C_V of K of tNAA were below 20% when 150 and 250 averages (scanning times of 7 and 11 min) were used in VOI_{PCC} and VOI_{CR}, respectively. Similar trends were observed for tCr and tCho (data not shown).

In addition, the diffusion metrics' variabilities as a function of the SNR estimated at b_0 are shown in Figure 4S of the Supplementary Material.

3.5 | Reproducibility and sample size analysis

C_R values for ADC_{exp} of all metabolites were calculated in VOI_{PCC} and VOI_{CR} for different acquisition schemes ($b_{[0,1,2]}$ and $b_{[0,2]}$) and acquisition times (12, 7, and 4 min), and reported as percentages of ADC_{exp} mean values (Table 3). The C_R were much lower in VOI_{PCC} than in VOI_{CR}, indicating higher repeatability in the first region. Interestingly, while C_R values for VOI_{CR} gradually increased when reducing the acquisition time, in VOI_{PCC} for all metabolites the C_R obtained for scheme $b_{[0,2]}$ and acquisition time of 4 min were smaller than those for the same scheme and acquisition time of 7 min.

For each of the acquisition schemes reported in Table 3, power calculations were performed for ADC_{exp} of tNAA to reflect the number of subjects per group required to detect a difference between two groups with a power of 80% and significance level of 5% (Figure 10). A 5% difference can be detected with 6 and 29 subjects per group in VOI_{PCC} and VOI_{CR}, respectively, with scheme $b_{[0,1,2]}$ and a scanning time of 12 min (Figure 10 A). With scheme $b_{[0,2]}$ and a scanning time of 7 min, a 5% difference can be detected with 17 and 29 subjects per group in VOI_{PCC} and in VOI_{CR}, respectively (Figure 10B). With $b_{[0,2]}$ and a reduced scanning time of 4 min, a 5% difference can be detected with 7 and 31 subjects per group in VOI_{PCC} and in VOI_{CR}, respectively (Figure 10C).

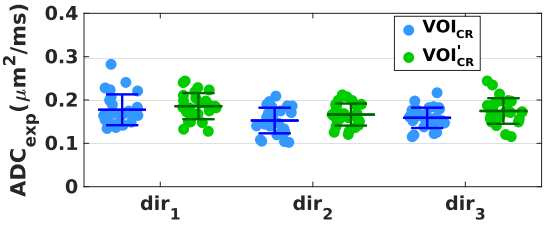

FIGURE 7 Effect of the voxel size on the variability of tNAA diffusion measures. ADC_{exp} derived from all subjects and sessions in VOI_{CR} and in VOI'_{CR}, displayed separately for each diffusion direction. Mean values (central bars) and SDs (outer bars) are plotted for each diffusion direction and VOI. ADC_{exp} values were estimated with scheme $b_{[0,2]}$ and 24 averages per diffusion condition in both voxels. Voxel sizes were the following: VOI_{CR}, 20 × 20 × 20 mm^3; VOI'_{CR}, 15 × 20 × 15 mm^3

TABLE 1 Mean SD and C_V of ADC_{exp}, ADC_K, and K values calculated for each session (S1 to S3) in VOI_{PCC} (scheme $b_{[0,1,2]}$ and 40 averages per diffusion condition)

Diffusion parameter	Metabolite	S1		S2		S3		Average	
		Mean (SD)	C_V (%)	Mean (SD)	C_V (%)	Mean (SD)	C_V (%)	Mean (SD)	C_V (%)
ADC_{exp} ($\mu m^2/ms$)	tNAA	0.126 (0.007)	6	0.120 (0.009)	7	0.124 (0.009)	7	0.123 (0.008)	7
	tCr	0.119 (0.010)	8	0.118 (0.013)	11	0.118 (0.010)	9	0.118 (0.011)	9
	tCho	0.106 (0.008)	8	0.106 (0.012)	12	0.107 (0.009)	9	0.106 (0.010)	9
	mIns	0.107 (0.015)	14	0.106 (0.015)	14	0.112 (0.015)	14	0.108 (0.015)	14
ADC_K ($\mu m^2/ms$)	tNAA	0.151 (0.011)	8	0.142 (0.014)	10	0.147 (0.014)	10	0.147 (0.013)	9
	tCr	0.141 (0.015)	11	0.139 (0.024)	18	0.135 (0.016)	12	0.140 (0.019)	13
	tCho	0.122 (0.012)	10	0.123 (0.020)	16	0.125 (0.013)	10	0.123 (0.015)	12
	mIns	0.134 (0.018)	14	0.133 (0.023)	17	0.141 (0.024)	17	0.136 (0.022)	16
K	tNAA	1.808 (0.204)	11	1.712 (0.211)	12	1.744 (0.266)	15	1.757 (0.227)	15
	tCr	1.689 (0.210)	12	1.692 (0.298)	18	1.552 (0.416)	27	1.645 (0.308)	19
	tCho	1.680 (0.486)	29	1.738 (0.262)	15	1.718 (0.291)	17	1.712 (0.346)	20
	mIns	1.533 (0.336)	22	1.522 (0.514)	34	1.817 (0.375)	21	1.624 (0.410)	25

TABLE 2 Average, SD, and C_V of ADC_{exp}, ADC_K, and K values calculated for each session (S1 to S3) in VOI_{CR} (scheme $b_{[0,1,2]}$ and 40 averages per diffusion condition) and average, SD, and C_V of ADC_{exp} calculated for each session in VOI'_{CR} (scheme $b_{[0,2]}$ and 24 averages per diffusion condition).

VOI_{CR}		S1		S2		S3		Average	
Diffusion parameter	Metabolite	Mean (SD)	C_V (%)	Mean (SD)	C_V (%)	Mean (SD)	C_V (%)	Mean (SD)	C_V (%)
ADC_{exp} ($\mu m^2/ms$)	tNAA	0.156 (0.017)	11	0.160 (0.020)	12	0.158 (0.020)	12	0.158 (0.019)	12
	tCr	0.156 (0.012)	7	0.174 (0.025)	14	0.173 (0.024)	14	0.168 (0.020)	12
	tCho	0.130 (0.015)	11	0.140 (0.025)	18	0.136 (0.023)	17	0.135 (0.023)	16
	mIns	0.126 (0.031)	22	0.156 (0.050)	32	0.130 (0.032)	24	0.137 (0.037)	27
ADC_K ($\mu m^2/ms$)	tNAA	0.186 (0.029)	16	0.180 (0.018)	10	0.189 (0.022)	12	0.185 (0.022)	12
	tCr	0.195 (0.025)	13	0.192 (0.031)	16	0.208 (0.026)	13	0.198 (0.031)	13
	tCho	0.162 (0.027)	16	0.146 (0.021)	15	0.156 (0.026)	17	0.155 (0.023)	15
	mIns	0.182 (0.033)	18	0.177 (0.056)	32	0.173 (0.036)	21	0.177 (0.039)	22
K	tNAA	1.308 (0.239)	18	1.238 (0.265)	21	1.190 (0.300)	25	1.246 (0.251)	20
	tCr	1.283 (0.243)	19	1.280 (0.218)	17	1.305 (0.192)	15	1.289 (0.204)	16
	tCho	1.507 (0.293)	19	1.166 (0.376)	32	1.238 (0.473)	38	1.304 (0.357)	27
	mIns	1.702 (0.425)	25	1.317 (0.230)	17	1.285 (0.453)	35	1.435 (0.346)	24
ADC_{exp} ($\mu m^2/ms$)	tNAA	0.185 (0.014)	8	0.179 (0.026)	15	0.163 (0.019)	12	0.176 (0.020)	11
	tCr	0.148 (0.029)	19	0.168 (0.022)	13	0.165 (0.027)	16	0.160 (0.026)	16
	tCho	0.130 (0.013)	10	0.137 (0.026)	19	0.127 (0.012)	9	0.132 (0.017)	13

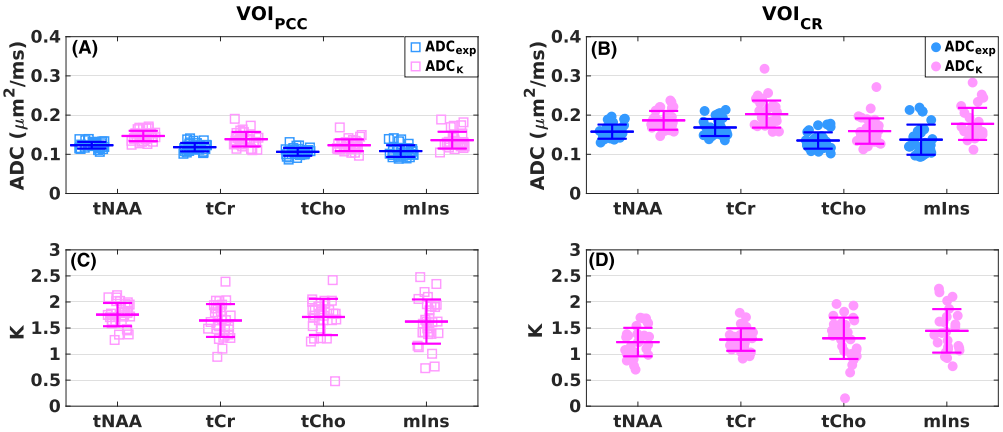

FIGURE 8 Inter-subject variability. ADC_{exp}, ADC_K, and K of all metabolites from all subjects and sessions derived in VOI_{PCC} (A, C) and VOI_{CR} (B, D) averaged over all diffusion directions. Mean values (central bars) and SDs (outer bars) are displayed for each parameter

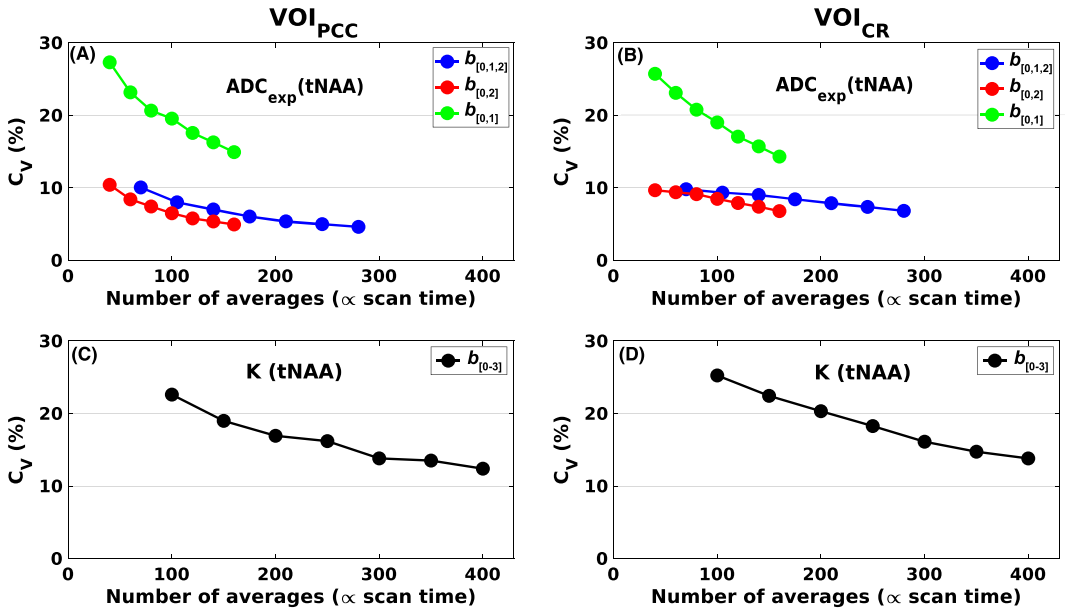

FIGURE 9 Intra-subject variability. Coefficients of variation for ADC_{exp} and K of tNAA, calculated in VOI_{PCC} (A, C) and in VOI_{CR} (B, D), from a bootstrapping subsampling procedure. The datasets from each subject and session were randomly resampled with replacement prior to averaging. Each subset consisted of 10, 15, 20, 25, 30, 35, and 40 averages per diffusion condition. The ADC_{exp} were estimated from different diffusion-weighting schemes: $b_{[0,1,2]}$, $b_{[0,2]}$, and $b_{[0,1]}$. The K were estimated using all b-values (scheme $b_{[0-3]}$)

TABLE 3 C_R and variance (σ^2) of ADC_{exp} values calculated for different acquisition schemes and acquisition times, in VOI_{PCC} and VOI_{CR}. Power analysis can be performed using the σ^2 values reported in the table and equation 4

		12 min acquisition (scheme $b_{[0,1,2]}$)		7 min acquisition (scheme $b_{[0,2]}$)		4 min acquisition (scheme $b_{[0,2]}$)	
VOI	Metabolite	C_R (% mean) ($\mu m^2/ms$)	σ^2 ($\times 10^{-4}$) ($\mu m^4/ms^2$)	C_R (%mean) ($\mu m^2/ms$)	σ^2 ($\times 10^{-4}$) ($\mu m^4/ms^2$)	C_R (%mean) ($\mu m^2/ms$)	σ^2 ($\times 10^{-4}$) ($\mu m^4/ms^2$)
VOI_{PCC}	tNAA	0.015 (12)	0.3	0.026 (20)	0.9	0.016 (13)	0.3
	tCr	0.023 (20)	0.7	0.032 (26)	1.3	0.030 (25)	1.1
	tCho	0.022 (20)	0.6	0.040 (37)	2.1	0.025 (23)	0.8
	mIns	0.040 (37)	2.1	0.066 (59)	5.7	0.050 (46)	3.3
VOI_{CR}	tNAA	0.042 (27)	2.3	0.042 (26)	2.3	0.045 (27)	2.6
	tCr	0.040 (24)	2.1	0.043 (25)	2.4	0.052 (29)	3.5
	tCho	0.044 (33)	2.6	0.046 (33)	2.7	0.050 (34)	3.2
	mIns	0.104 (75)	14.1	0.085 (62)	9.4	0.101 (67)	13.4

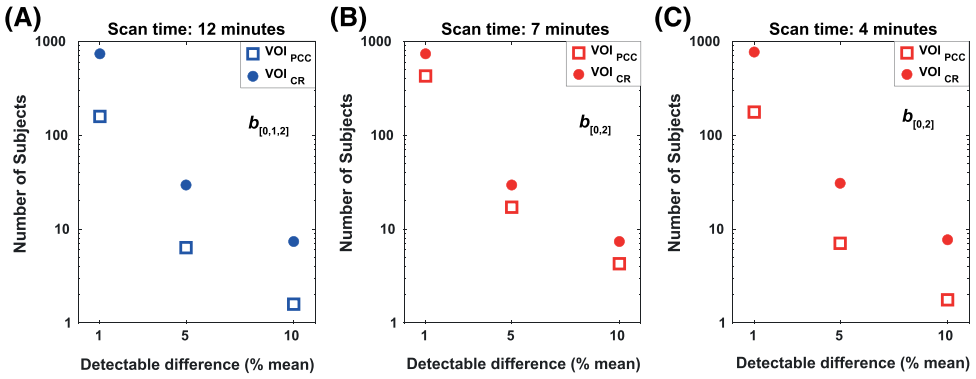

FIGURE 10 Reproducibility analysis. Number of subjects (per group) required to detect a difference in the ADC_{exp} of tNAA (as a percentage of the mean) with significance level $\alpha = 0.05$ and power of $1 - \beta = 0.80$. The power was calculated in VOI_{PCC} and VOI_{CR} for the full dataset including all b-values up to $b_2 = 3300$ s/mm^2 (scheme $b_{[0,1,2]}$), corresponding to an acquisition time of 12 min (a), and sub-sampled datasets using $b_0 = 11$ s/mm^2 and $b_2 = 3300$ s/mm^2 (scheme $b_{[0,2]}$) and different numbers of averages (B, C), corresponding to acquisition times of 7 and 4 min, respectively

In addition, C_R values for K of all metabolites were calculated in VOI_{PCC} and VOI_{CR} and reported as percentages of the K mean values (Table 4S, Supplementary Material). The power calculation for tNAA K revealed that a 10% difference can be observed with 11 and 21 subjects per group in VOI_{PCC} and VOI_{CR}, respectively.

4 | DISCUSSION

The variability of metabolite diffusion parameters measured with DW-semi-LASER across different subjects and sessions was evaluated in two brain regions of interest (PCC and CR) and with different acquisition and post-processing strategies. Our data showed that DW-MRS is feasible at 3 T with an excellent statistical power even employing a short acquisition protocol in small subject populations, providing that the proper choice of b-values, the execution with cardiac triggering, and the post-processing with peak thresholding are all taken carefully into account. The optimized acquisition and analysis pipeline allowed to obtain high quality DW-MR spectra for all subjects, sessions and VOIs, up to the highest b-value of b = 7300 s/mm^2 (Figure 2B and 2D), enabling the utilization of this method in clinically feasible acquisition times.

Nevertheless, the variance of the diffusion measures differed significantly across brain regions (despite the similar SNR at b_0), as they are affected by motion artifacts to different extents, and also depended on the VOI size: while acquisitions in a larger VOI provide higher SNR, a smaller VOI may allow for more robust datasets and lower variability of the diffusion measures.

From power calculations we estimated that, under our experimental conditions, 5% differences in tNAA mean diffusion coefficient can be detected with a sample size of 7 and 31 subjects per group in the PCC and in the CR, respectively, with an acquisition time of 4 min. Remarkably, the measure of metabolite diffusion parameters was extremely robust and reproducible in the PCC, while much higher variability was observed in the CR when the VOI was located next to the ventricles.

4.1 | Effect of physiological motion on the DW signal

Potential sources of bias in the evaluation of metabolite ADCs were identified, mainly attributed to the effect of physiological motion on the DW signal. Whilst artifacts induced by pure translational motion can be corrected by properly adjusting the frequency and phase of the single averages before summation, small rotations or compressive motions due to cardiac and cerebrospinal fluid pulsation may induce severe amplitude drops that are more difficult to address.[4]

To evaluate the effect of physiological motion on the DW signal, in one subject we investigated the influence of cardiac gating on tNAA SNR over time and across different directions. The mean normalized signal was higher when the acquisition was synchronized to the cardiac cycle at all b-values, while the associated SDs were always lower except for one condition (b = 850 s/mm^2, dir_2) (Figure 4C). This result highlights the importance of employing cardiac gating in DW-MRS experiments with high b-values, and the fact that the proximity of the VOI to the ventricles may be detrimental for the DW signal. However, the assessment of the optimal trigger delay would require a more systematic investigation, since it may depend on the region of interest, DW-MRS sequence parameters, and cardiac gating device utilized. One possible limitation of using cardiac gating is that the effective T_R is slightly variable during the acquisition, thus possibly introducing another source of ADC variability. Moreover, it may differ from subject to subject, depending on the individual heart rate. Nevertheless, the intra-subject T_R fluctuations induced by irregular heart beatings were a source of smaller signal amplitude variability compared with that observed without cardiac synchronization (Figure 4C).

In a previous study, the metabolite-cycling method and the use of the inherent water peak were proposed for compensation of significant signal loss.[37] Peak thresholding represents an alternative way to overcome the issue of motion-related signal amplitude fluctuations, and becomes crucial especially at high diffusion-weighting values. This procedure avoids the risk of artificial overestimation of ADCs as a consequence of underestimation of the DW signal in the presence of significant drops in the signal amplitude due to non-translational motion. Although the removal of some of the spectra before averaging could introduce a relatively small artificial increase of SNR (see Supplementary Material S1), as expected, in both VOIs the variability of ADCs across subjects and sessions was lower when peak thresholding was applied (Figure 6). Notably, the effect of peak thresholding was more pronounced in VOI_{CR} than VOI_{PCC}, suggesting that motion affects the diffusion-sensitized signal in the parietal WM more than in the PCC. In addition, the variability of the ADCs was much higher in two of the three DW directions (dir_1 and dir_2) in VOI_{CR} (Figure 6), indicating that motion is associated preferentially with specific directions, while in VOI_{PCC} there was no significant difference among directions. Interestingly, the ADC variability in the smaller voxel VOI'_{CR} did not depend on the diffusion direction (Figure 7), and, despite the intrinsic lower SNR related to voxel size, the ADC variability in VOI'_{CR} was lower than that in VOI_{CR} in dir_1 and dir_2, suggesting that in these directions the effect of motion is dominant with respect to noise, thus affecting to a greater extent the larger VOI. In addition, the average number of rejected spectra after peak thresholding was smaller in VOI'_{CR} than in VOI_{CR}, further corroborating this hypothesis.

4.2 | Metabolite kurtosis analysis

Diffusion-attenuation curves were fitted to mono-exponential functions up to b_2 = 3300 s/mm^2 and to a kurtosis model (Equation 2) up to b_3 = 7300 s/mm^2. The χ^2 goodness-of-fit test revealed that the mono-exponential fit was not able to explain 30% of the metabolite signal decays up to b_3, whereas the kurtosis approach was found to be more accurate (the null hypothesis was accepted for all fits with $p > 0.9$). The non-mono-exponential behavior of the signal decay at high *b*-values may originate from non-gaussian, restricted diffusion within individual compartments, distributions of diffusion coefficients associated with multiple gaussian compartments, fiber dispersion, exchange effects, or a combination of these processes.[38] Sampling DW-MRS data at high *b*-values is necessary to derive information on tissue morphology at the microscopic scale.[6,39] Although reaching ultra-high *b*-values greater than 15000 s/mm^2 would be desirable for accurate modeling of DW-MRS signals and extraction of microstructural parameters, this may be very challenging in a clinical context with stringent limitations in the acquisition times. In the present study, we evaluated the possibility of capturing deviations from mono-exponentiality using the kurtosis approach, with a reasonably high *b*-value of 7300 s/mm^2 and a relatively short acquisition protocol. Significantly higher *K* mean values in GM compared with WM for all metabolites confirmed previous results suggesting greater diffusional heterogeneity in GM.[40] Coefficients of variation for *K* were much higher than those obtained for the ADCs.

4.3 | Inter-subject and intra-subject variability

The inter-subject variability calculated from full datasets was less than 16% for ADC_{exp} and ADC_K of all metabolites under investigation in VOI_{PCC} (Table 1), while it was higher in VOI_{CR} (<16% for tNAA, tCr, and tCho, <27% for mIns) (Table 2). In contrast, the inter-subject variability of *K* was less than 27% for all metabolites in both VOIs.

The robustness of the DW-MRS acquisition was evaluated by exploring the variability of the diffusion measures associated with different sub-samplings of the data. The procedure was repeated for different numbers of averages per DW condition and different diffusion-weighting schemes, corresponding to different acquisition times. In both VOIs, the coefficients of variation for tNAA, tCr, and tCho ADCs were lower than 10% when 60 or more averages were considered using scheme $b_{[0,2]}$, corresponding to acquisition times of at least 3 min (Figure 9A and 9B). With scheme $b_{[0,1,2]}$, the same variability could be reached with at least 90 averages, indicating that acquiring spectra at the low *b*-value of 850 s/mm^2 does not add stability to the ADC calculation. Finally, using scheme $b_{[0,1]}$ should be avoided, since it does not provide sufficient diffusion-weighting for proper ADC estimations. Figure 4S (Supplementary Material) shows the behavior of the diffusion metrics' variabilities as a function of the SNR estimated at b_0. These plots report the non-DW SNR necessary to obtain a certain variability of the diffusion measures in the brain regions under investigation, providing that all acquisition and post-processing steps are properly performed, and can be useful to translate our results to data acquired on different experimental setups. However, depending on the effect of motion and other factors such phase and amplitude fluctuations on the DW signal detected in the region of interest, the SNR at b_0 cannot be directly linked to the robustness of the measurements, and these results should be adapted with caution to different experimental conditions.

DW-MRS can be used to characterize microstructural alterations affecting brain tissue in a variety of diseases. Previous clinical and preclinical studies reported differences greater than 20% in the diffusion of several metabolites in patients with ischemic stroke or tumor, compared with healthy subjects.[41,42] Wood et al reported differences of almost 20% in the tNAA diffusivity in the corpus callosum of patients with multiple sclerosis,[13] while differences in tCho and tCr ADCs of more than 15% were observed in systemic lupus erythematosus.[11] Our results on ADC_{exp} repeatability (Table 3) suggest that for investigation of tNAA, tCr, tCho, and mIns diffusion abnormalities in pathologies where the expected ADC_{exp} differences are greater than 10%, it is sufficient to keep the acquisition time per region of interest below 5 min, with a group size of about 30 subjects. In contrast, to explore more subtle microstructural abnormalities in normal aging or neurological diseases at the very early stage, longer acquisition times are probably desirable, and need to be evaluated case by case depending on the location and size of the brain region under investigation and the expected differences in the diffusion metrics.

5 | CONCLUSIONS

We have evaluated the performance of a DW-semi-LASER sequence at 3 T and demonstrated the feasibility of this method in a clinical setting, providing that all procedures from experimental planning (choice of *b*-values and number of averages), execution (cardiac triggering), and post-processing (peak thresholding in addition to standard phase and frequency corrections) are carefully performed. Altered metabolite diffusion in tissue has been shown to reflect specific structural damage in disease. In particular, the diffusion of the neuronal marker tNAA has been suggested to reflect pure intra-axonal damage in WM diseases, while the diffusion of tCho and tCr represents potential markers of inflammation and glial cell alterations. DW-semi-LASER may allow the exploration of microscopic cellular alterations in different pathological conditions, providing useful insights into the pathogenesis and evolution of the disease, and eventually helping to choose the most appropriate temporal window for tailored therapies and to monitor treatment response.

FUNDING INFORMATION

This work was supported by the programs 'Institut des neurosciences translationnelle' (ANR-10-IAIHU-06) and 'Infrastructure d'avenir en Biologie Santé' (ANR-11-INBS-0006). Małgorzata Marjańska and Edward J. Auerbach acknowledge the support of NIH grants (BTRC P41 EB015894 and P30 NS076408).

ORCID

Małgorzata Marjańska https://orcid.org/0000-0002-4727-2447
Francesca Branzoli https://orcid.org/0000-0001-9792-0492

References

1. Cao P, Wu EX. *In vivo* diffusion MRS investigation of non-water molecules in biological tissues. *NMR Biomed*. 2017;30(3):e3481.
2. Nicolay K, Braun KPJ, de Graaf RA, Dijkhuizen RM, Kruiskamp MJ. Diffusion NMR spectroscopy. *NMR Biomed*. 2001;14(2):94-111.
3. Palombo M, Shemesh N, Ronen I, Valette J. Insights into brain microstructure from in vivo DW-MRS. *Neuroimage*. 2018;182:97-116.
4. Ronen I, Valette J. Diffusion-weighted magnetic resonance spectroscopy. In: Harris RK, Wasylishen RL, eds. *EMagRes*. Chichester, UK: Wiley; 2015:733-750.
5. Palombo M, Ligneul C, Najac C, et al. New paradigm to assess brain cell morphology by diffusion-weighted MR spectroscopy in vivo. *Proc Natl Acad Sci U S A*. 2016;113(24):6671-6676.
6. Palombo M, Ligneul C, Hernandez-Garzon E, Valette J. Can we detect the effect of spines and leaflets on the diffusion of brain intracellular metabolites? *Neuroimage*. 2018;182:283-293.
7. Shemesh N, Rosenberg JT, Dumez J-N, Muniz JA, Grant SC, Frydman L. Metabolic properties in stroked rats revealed by relaxation-enhanced magnetic resonance spectroscopy at ultrahigh fields. *Nat Commun*. 2014;5(1):4958-4966.
8. Shemesh N, Rosenberg JT, Dumez J-N, Grant SC, Frydman L. Distinguishing neuronal from astrocytic subcellular microstructures using *in vivo* Double Diffusion Encoded ^{1}H MRS at 21.1 T. *Plos ONE*. 2017;12(10):e0185232.
9. Valette J, Ligneul C, Marchadour C, Najac C, Palombo M. Brain metabolite diffusion from ultra-short to ultra-long time scales: what do we learn, where should we go? *Front Neurosci*. 2018;12:2-8.
10. Branzoli F, Ercan E, Valabrègue R, et al. Differentiating between axonal damage and demyelination in healthy aging by combining diffusion-tensor imaging and diffusion-weighted spectroscopy in the human corpus callosum at 7 T. *Neurobiol Aging*. 2016;47:210-217.
11. Ercan E, Magro-Checa C, Valabregue R, et al. Glial and axonal changes in systemic lupus erythematosus measured with diffusion of intracellular metabolites. *Brain*. 2016;139(5):1447-1457.
12. Ligneul C, Palombo M, Hernández-Garzón E, et al. Diffusion-weighted magnetic resonance spectroscopy enables cell-specific monitoring of astrocyte reactivity in vivo. *Neuroimage*. 2019;191:457-469.
13. Wood ET, Ronen I, Techawiboonwong A, et al. Investigating axonal damage in multiple sclerosis by diffusion tensor spectroscopy. *J Neurosci*. 2012;32(19):6665-6669.
14. Posse S, Cuenod CA, Le Bihan D. Human brain: proton diffusion MR spectroscopy. *Radiology*. 1993;188:719-725.
15. Frahm J, Bruhn H, Gyngell ML, Merboldt KD, Hänicke W, Sauter R. Localized high-resolution proton NMR spectroscopy using stimulated echoes: initial applications to human brain in vivo. *Magn Reson Med*. 1989;9(1):79-93.
16. Bottomley PA. Spatial localization in NMR spectroscopy in vivo. *Ann N Y Acad Sci*. 1987;508:333-348.
17. Garwood M, DelaBarre L. The return of the frequency sweep: designing adiabatic pulses for contemporary NMR. *J Magn Reson*. 2001;153(2):155-177.
18. Branzoli F, Ercan E, Webb A, Ronen I. The interaction between apparent diffusion coefficients and transverse relaxation rates of human brain metabolites and water studied by diffusion-weighted spectroscopy at 7 T. *NMR Biomed*. 2014;27(5):495-506.
19. Najac C, Branzoli F, Ronen I, Valette J. Brain intracellular metabolites are freely diffusing along cell fibers in grey and white matter, as measured by diffusion-weighted MR spectroscopy in the human brain at 7 T. *Brain Struct Funct*. 2016;221(3):1245-1254.
20. Deelchand DK, Auerbach EJ, Marjańska M. Apparent diffusion coefficients of the five major metabolites measured in the human brain in vivo at 3T: ADC of human brain metabolites at 3T. *Magn Reson Med*. 2018;79(6):2896-2901.
21. Scheenen TWJ, Klomp DWJ, Wijnen JP, Heerschap A. Short echo time ^{1}H-MRSI of the human brain at 3T with minimal chemical shift displacement errors using adiabatic refocusing pulses. *Magn Reson Med*. 2008;59(1):1-6.
22. Andronesi OC, Ramadan S, Ratai E-M, Jennings D, Mountford CE, Sorensen AG. Spectroscopic imaging with improved gradient modulated constant adiabaticity pulses on high-field clinical scanners. *J Magn Reson*. 2010;203(2):283-293.
23. Wood ET, Ercan AE, Branzoli F, et al. Reproducibility and optimization of *in vivo* human diffusion-weighted MRS of the corpus callosum at 3T and 7T. *NMR Biomed*. 2015;28(8):976-987.
24. Ellegood J, Hanstock CC, Beaulieu C. Trace apparent diffusion coefficients of metabolites in human brain using diffusion weighted magnetic resonance spectroscopy. *Magn Reson Med*. 2005;53(5):1025-1032.
25. Zheng G, Price WS. Suppression of background gradients in (B_0 gradient-based) NMR diffusion experiments. *Concepts Magn Reson A*. 2007;30A(5):261-277.
26. Tkac I, Starcuk Z, Choi I-Y, Gruetter R. In vivo ^{1}H NMR spectroscopy of rat brain at 1 ms echo time. *Magn Reson Med*. 1999;41:649-656.

27. Tkac I, Gruetter R. Methodology of ^{1}H NMR spectroscopy of the human brain at very high magnetic fields. *Appl Magn Reson*. 2005;29:139-157.
28. Gruetter R, Tkáč I. Field mapping without reference scan using asymmetric echo-planar techniques. *Magn Reson Med*. 2000;43(2):319-323.
29. de Brouwer H. Evaluation of algorithms for automated phase correction of NMR spectra. *J Magn Reson*. 2009;201(2):230-238.
30. Provencher SW. Estimation of metabolite concentrations from localized in vivo proton NMR spectra. *Magn Reson Med*. 1993;30(6):672-679.
31. Henry P-G, Marjanska M, Walls JD, Valette J, Gruetter R, Ugurbil K. Proton-observed carbon-edited NMR spectroscopy in strongly coupled second-order spin systems. *Magn Reson Med*. 2006;55(2):250-257.
32. Govindaraju V, Young K, Maudsley AA. Proton NMR chemical shifts and coupling constants for brain metabolites. *NMR Biomed*. 2000;13:129-153.
33. Kaiser LG, Marjańska M, Matson GB, et al. ^{1}H MRS detection of glycine residue of reduced glutathione *in vivo*. *J Magn Reson*. 2010;202(2):259-266.
34. Jensen JH, Helpern JA, Ramani A, Lu H, Kaczynski K. Diffusional kurtosis imaging: the quantification of non-gaussian water diffusion by means of magnetic resonance imaging. *Magn Reson Med*. 2005;53(6):1432-1440.
35. Yablonskiy DA, Sukstanskii AL. Theoretical models of the diffusion weighted MR signal. *NMR Biomed*. 2010;23(7):661-681.
36. Bartlett JW, Frost C. Reliability, repeatability and reproducibility: analysis of measurement errors in continuous variables. *Ultrasound Obstet Gynecol*. 2008;31(4):466-475.
37. Döring A, Adalid V, Boesch C, Kreis R. Diffusion-weighted magnetic resonance spectroscopy boosted by simultaneously acquired water reference signals. *Magn Reson Med*. 2018;80(6):2326-2338.
38. Henriques RN, Jespersen SN, Shemesh N. Microscopic anisotropy misestimation in spherical-mean single diffusion encoding MRI. *Magn Reson Med*. 2019;81(5):3245-3261.
39. Palombo M, Ligneul C, Valette J. Modeling diffusion of intracellular metabolites in the mouse brain up to very high diffusion-weighting: diffusion in long fibers (almost) accounts for non-monoexponential attenuation. *Magn Reson Med*. 2017;77(1):343-350.
40. Ingo C, Brink W, Ercan E, Webb AG, Ronen I. Studying neurons and glia non-invasively via anomalous subdiffusion of intracellular metabolites. *Brain Struct Funct*. 2018;223(8):3841-3854.
41. Harada M, Uno M, Hong F, Hisaoka S, Nishitani H, Matsuda T. Diffusion-weighted in vivo localized proton MR spectroscopy of human cerebral ischemia and tumor. *NMR Biomed*. 2002;15(1):69-74.
42. Zheng DD, Liu ZH, Fang J, Wang XY, Zhang J. The effect of age and cerebral ischemia on diffusion-weighted proton MR spectroscopy of the human brain. *Am J Neuroradiol*. 2012;33(3):563-568.

SUPPORTING INFORMATION

Additional supporting information may be found online in the Supporting Information section at the end of the article.

How to cite this article: Genovese G, Marjańska M, Auerbach EJ, et al. In vivo diffusion-weighted MRS using semi-LASER in the human brain at 3 T: Methodological aspects and clinical feasibility. *NMR in Biomedicine*. 2021;34:e4206. https://doi.org/10.1002/nbm.4206